CHEMISTRY

Magnetic molecular orbitals in MnSi

Zhendong Jin[1]†, Yangmu Li[2,3,4]†, Zhigang Hu[1]†, Biaoyan Hu[1], Yiran Liu[1], Kazuki Iida[5], Kazuya Kamazawa[5], Matthew B. Stone[6], Alexander I. Kolesnikov[6], Douglas L. Abernathy[6], Xiangyu Zhang[7], Haiyang Chen[7], Yandong Wang[7], Chen Fang[2,8,9], Biao Wu[1,10], Igor A. Zaliznyak[3], John M. Tranquada[3], Yuan Li[1,11]*

A large body of knowledge about magnetism is attained from models of interacting spins, which usually reside on magnetic ions. Proposals beyond the ionic picture are uncommon and seldom verified by direct observations in conjunction with microscopic theory. Here, using inelastic neutron scattering to study the itinerant near-ferromagnet MnSi, we find that the system's fundamental magnetic units are interconnected, extended molecular orbitals consisting of three Mn atoms each rather than individual Mn atoms. This result is further corroborated by magnetic Wannier orbitals obtained by ab initio calculations. It contrasts the ionic picture with a concrete example and presents an unexplored regime of the spin waves where the wavelength is comparable to the spatial extent of the molecular orbitals. Our discovery brings important insights into not only the magnetism of MnSi but also a broad range of magnetic quantum materials where structural symmetry, electron itinerancy, and correlations act in concert.

INTRODUCTION

It is intuitive to use networks of interacting spins to describe magnetism in insulators, yet even for itinerant systems such as semiconductors (*1*) and metals (*2*), the notion of interacting moments sitting on real-space lattice sites remains useful. Spins are usually identified with magnetic ions, which correspond to tight-binding electronic models constructed from atomic orbitals. However, the ionic picture is not always accurate. Pauling (*3*) first pointed out that covalent bonding alters transition metals' electron count and moment compared to the ionic case. A modern insight into the problem can be obtained by considering the notion of Wannier orbitals, computable as maximally localized Wannier functions (MLWFs) (*4*), which replace atomic orbitals and form a natural basis for low-energy tight-binding models (*5*–*7*). They also describe magnetic electron clouds with unpaired spins (*4*, *8*). While exponentially localized and symmetric Wannier orbitals generally exist in "topologically trivial" materials (*9*, *10*), they are not always centered on atomic sites (*11*–*13*). For instance, when tightly bonded clusters of atoms are embedded in a loosely bonded matrix (*14*–*16*), electrons can become partially delocalized on the clusters but have weak intercluster hopping, forming molecular orbitals. Magnetic molecular orbitals are recently considered a fertile ground for finding new quantum magnets (*17*).

The formation of molecular orbitals can also be an emergent phenomenon without a cluster-like structural motif. In such cases, they can be mathematically distinguished by their off-atom Wannier centers (*11*, *12*), of which an instructive (nonmagnetic) example is silicon, where the valence electrons are centered on Si-Si bonds (*12*, *13*, *18*). These interconnected molecular orbitals are characteristic of electron delocalization in covalent solids, to which many transition metal compounds actually belong, at least partially (*8*, *19*). When a correlated metal's electronic interaction strength is continuously tuned toward a Mott transition, one can imagine a state where molecular orbitals form out of a balance between electronic interactions and kinetic energy. To give some examples, benzene-like magnetic molecular orbitals have been theoretically proposed in 4d and 5d transition metal oxides with a honeycomb lattice (*20*–*22*), challenging some of the materials' potential to realize the Kitaev model (*23*). Orbital loop currents proposed in cuprate (*24*) and kagome (*25*) superconductors can be viewed as molecular orbitals with unquenched orbital magnetic moments. Recent neutron scattering experiments in iron chalcogenide superconductors have indicated the presence of unusual magnetic plaquettes (*26*), which are consistent with magnetic molecular orbitals despite the fact that their formation mechanism is not clearly understood (*27*). Establishing an emergent magnetic molecular orbital reality can thus be expected to fundamentally influence research in a broad range of correlated electron systems.

Here, we present a discovery of interconnected emergent magnetic molecular orbitals in a simple binary compound MnSi using inelastic neutron scattering (INS). The central idea stems from the concept of magnetic form factor, which is a momentum-dependent prefactor of the magnetic neutron scattering cross section (*28*), given by the Fourier transform of the electron cloud associated with each spin. The key is that the form factor of a magnetic molecular orbital has distinct structures that can be experimentally observed. MnSi hosts intriguing physics including chiral magnetism (*29*) and electronic nodal planes (*30*, *31*) due to its

[1]International Center for Quantum Materials, School of Physics, Peking University, Beijing 100871, China. [2]Beijing National Laboratory for Condensed Matter Physics and Institute of Physics, Chinese Academy of Sciences, Beijing 100190, China. [3]Condensed Matter Physics and Materials Science Division, Brookhaven National Laboratory, Upton, NY 11973, USA. [4]School of Physical Sciences, University of Chinese Academy of Sciences, Beijing 100049, China. [5]Neutron Science and Technology Center, Comprehensive Research Organization for Science and Society (CROSS), Tokai 319-1106, Ibaraki, Japan. [6]Neutron Scattering Division, Oak Ridge National Laboratory, Oak Ridge, TN 37831, USA. [7]State Key Laboratory for Advance Metals and Materials, University of Science and Technology Beijing, Beijing 10083, China. [8]Songshan Lake Materials Laboratory, Dongguan, Guangdong 523808, China. [9]Kavli Institute for Theoretical Sciences, Chinese Academy of Sciences, Beijing 100190, China. [10]Wilczek Quantum Center, School of Physics and Astronomy, Shanghai Jiao Tong University, Shanghai 200240, China. [11]Tsung-Dao Lee Institute and School of Physics and Astronomy, Shanghai Jiao Tong University, Shanghai 200240, China.
*Corresponding author. Email: yuan.li@pku.edu.cn
†These authors contributed equally to this work.

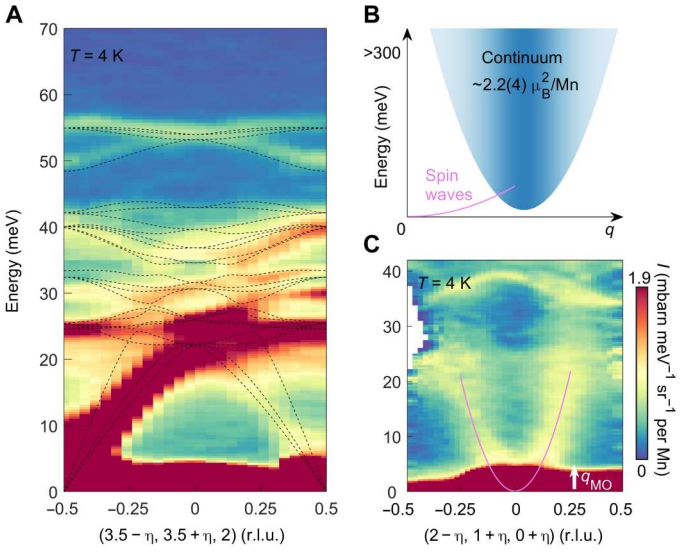

Fig. 1. Overview of INS signals. (**A**) Phonons measured in high-index BZs. DFT-calculated dispersions are shown as dashed lines. (**B**) Schematic of magnetic excitations, including spin waves and a continuum up to high energies with substantial spectral weight (estimated without form factor reduction; see the Supplementary Materials). (**C**) Spin waves in the (2,1,0) BZ. The signal becomes weak beyond $q_{MO} \approx 0.65$ Å^{-1} from the zone center (figs. S4 and S5). Phonons are visible above ~20 meV (fig. S4). Magenta lines are spin-wave dispersions (*32*).

noncentrosymmetric and nonsymmorphic crystal structure (fig. S1), yet its advantage for our purpose is its itinerant magnetism (*29*, *32*): Magnetic excitations of MnSi are well characterized (*32*), hence allowing for a definitive measurement of the magnetic form factor (*8*, *19*). The electronic structure can be reliably calculated with density functional theory (DFT) (*30*, *33*), which enables the calculation of the Wannier orbitals. Combined together, our results conclusively show that the fundamental magnetic units of MnSi are extended molecular orbitals instead of atomic orbitals of individual Mn.

RESULTS

To begin, we present in Fig. 1A our INS measurement of phonons using a 33-g twin-free single-crystal sample (fig. S2). DFT-calculated phonon dispersions are overlaid with the data and show very good agreement. With this information, we can then identify magnetic signals by avoiding the phonons in momentum (**Q**) and energy (*E*) transfer. Figure 1B illustrates the two types of magnetic signals that we observe. First, at high energy, there is a continuum of excitations carrying a substantial spectral weight, which appears to be a common feature of itinerant ferromagnets (*34*, *35*). The wide energy span (≥300 meV) of the excitations suggests that they are related to conduction electrons, whose bandwidths are more than 1 eV (*30*, *33*). Second, at low energies and emanating from the Brillouin zone (BZ) center, there are (nearly) ferromagnetic spin waves with a parabolic dispersion (*36*). These modes are damped because of coupling to the conduction electrons (*32*). Consistent with a recent report (*35*), we observe the spin waves in the BZ of (2,1,0) [in reciprocal lattice units (r.l.u.)], where phonon signals are weak (Fig. 1C). The spin-wave dispersion is distinct from the phonons and can be observed in other BZs (fig. S3). As has been previously found (*32*, *35*), both the spin waves (paramagnons) and the continuum persist far above the magnetic ordering temperature of 29.5 K (figs. S7 and S8).

Figure 2A displays the excitation continuum at energies higher than the phonon bands. The observed **Q**-space structures are nearly independent of *E* (up to at least 250 meV; see figs. S6 and S7), presumably because the measured energy window is narrow compared to the conduction bandwidth. The continuum's intensity varies between the BZs, and within the BZ of (2,1,0), it can be approximately described by a thick spherical shell ("shell model" hereafter) of a diameter slightly greater than 1 r.l.u. (Fig. 2B). Shells belonging to adjacent BZs are merged together, leaving holes around the X points of the BZ (Fig. 2C). The shell model is also consistent with signals coming from the energy minimum of the continuum, which we observe as broad features near the R and M points in Fig. 2D, below the phonon and the spin-wave dispersions, consistent with the expectation based on the Stoner theory (*32*). In fig. S9 (see the Supplementary Materials), we show that this low-energy signal varies across the BZs in the same way as the high-energy continuum. In contrast, the spin waves and the continuum have different intensity variation across the BZs (Figs. 1C and 2D; see also fig. S10), which implies that different descriptions are needed for the coherent scattering.

We now use the diffuse and dispersion-less continuum as a probe of the magnetic form factor, which we expect to be encoded in the inter-BZ intensity variations. The wide energy bandwidth enables us to access a wide **Q** range and corroborate the data consistency (figs. S6, S7, and S11). Figure 3A presents the radial *Q* dependence of the signal after averaging over all directions in **Q**. Unexpectedly, the intensity exhibits a distinct local maximum at $Q_0 = 2.5$ Å^{-1}, rather than being a monotonically decreasing function of *Q* as expected for the atomic form factor (*28*). This local maximum immediately suggests that the magnetization cloud has an internal characteristic length of $\sim 2\pi/Q_0$. The intensity exhibits rich inter-BZ variations (Fig. 3, B and C), including a pronounced directional dependence (Fig. 3D) on the momentum sphere $|\mathbf{Q}| = Q_0$.

Despite the apparent complexity, all of the above **Q** dependence can be quantitatively captured by a simple and intuitive model for the magnetic form factor. To introduce the model, we note that the DFT-calculated magnetization density (Fig. 3F) is concentrated around the Mn atoms, which can be organized into nearest-neighbor equilateral triangles (labeled as NNET in the figures) perpendicular to the four ⟨111⟩ directions (Fig. 3G and fig. S1). This suggests a model where an individual triangle is the fundamental magnetic unit. In our model, each spin is assumed to reside equally on all three vertices of an individual triangle (side = 2.8 Å, close to $2\pi/Q_0$). By computing the form factor of the triangles averaged over the four orientations (Fig. 3G) and using the result in the shell model (Fig. 2C), which we discuss in detail in the Supplementary Materials, we obtain an excellent description of the **Q**-dependent intensities of the continuum (Fig. 3, A to E). The only fit parameters are a background constant, an overall intensity scale, and the diameter and Gaussian thickness of the intra-BZ shells. The inclusion of the shell model has nearly no effect on the calculation in Fig. 3A (NNET), and it only adds periodic fine details to the results in Fig. 3 (B, C, and E). The inter-BZ variations entirely arise from the form factor of the triangles (fig. S15), which has no adjustable parameter and very little dependence on the description of the

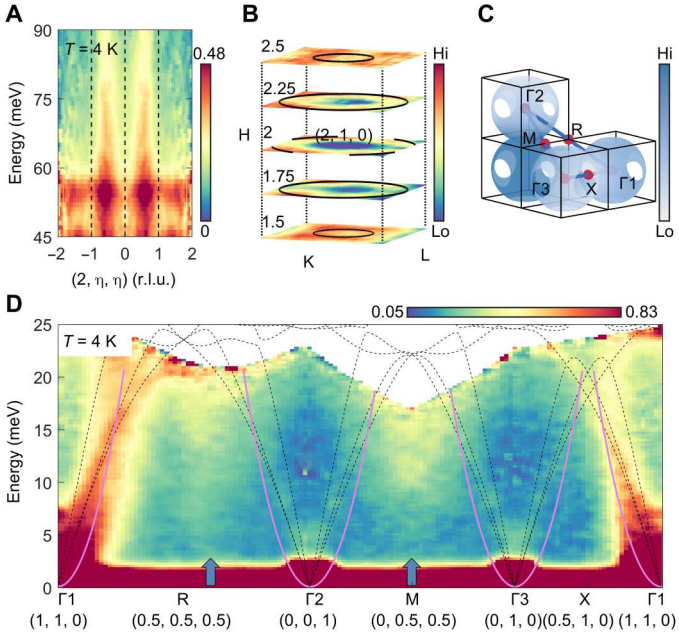

Fig. 2. Momentum structure of excitation continuum. (**A**) Nearly energy-independent spectra above phonon energies. (**B**) Intra-BZ structure measured at 70 ± 10 meV in the (2,1,0) BZ, normalized in each constant *H* slice. Black circles represent a sphere of radius 0.76 Å^{-1} (shell modelin the Results section). (**C**) Connected spherical shells over several BZs. Calculated scattering cross section (Fig. 3) is displayed in gray scale. (**D**) Low-energy spectra along the **Q** trajectory indicated in (C). The bottom of the continuum (arrows) is seen near the M and R points, below the phonon (black dotted lines) and spin-wave (magenta lines) dispersions.

magnetization densities on Mn (fig. S16). To assess whether the form factor associated with the triangle cluster is uniquely favored, alternative clusters of different sizes have been tested (figs. S12 to S14). None of them can describe the data as satisfactorily as the triangles (Fig. 3A). The form factor of the triangles is able to describe the global intensity variations of the continuum, down to its energy minimum and into the first BZ (Fig. 2, C and D, and figs. S16 and S17). To further demonstrate the necessity of the triangles, we present a comparison to simulations using generalized atomic form factors, $f_{Mn^{2+}}(p_{cov}Q)$, where p_{cov} is an adjustable "covalent" factor that represents increased spatial extent of magnetization density near the Mn atoms. By using p_{cov} = 1 and 2 to represent the localized and itinerant limits (fig. S19), respectively, we show that, in both limits, the model fails to describe our INS data (Fig. 3, A to C). In particular, the intensity's local maximum near Q_0 is missing from such models.

The success of the form factor of the triangles indicates that the individual magnetization clouds are molecular orbitals centered between atoms, which reflect the fact that the magnetization density islands in Fig. 3F are organized into triangles, over which neutrons scatter coherently. The coherence arises from the hybridization of magnetic electrons' wave functions and is distinct from magnetic correlations between neighboring Mn atoms enforced by ferromagnetic interactions: The strength of the interactions would have to be unrealistically large to support dynamic correlations at hundreds of millielectron volt. To elucidate the electronic structure behind the molecular orbitals, we examine the eight magnetic conduction bands (Fig. 4A) crossing the Fermi level (E_F). Symmetry analysis (table S1) shows that these bands form an elementary band representation (EBR), which opens up the possibility

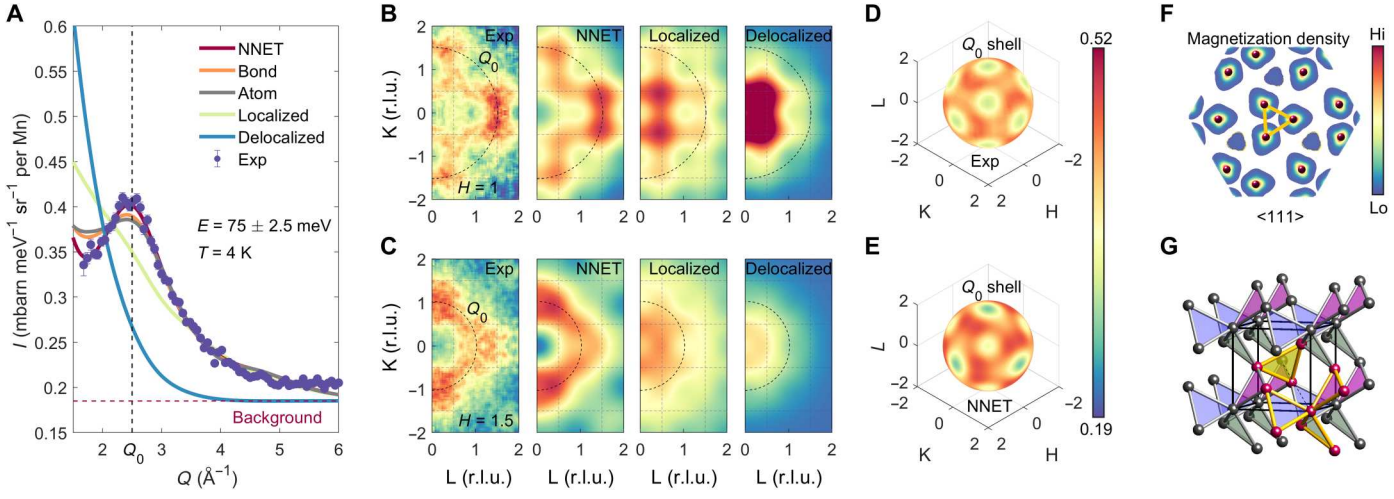

Fig. 3. Model for magnetic form factor. (**A**) Radial intensity distribution of the continuum, after averaging over all directions in **Q**. Q_0 = 2.5 Å^{-1} indicates a local maximum. Magnetic clusters centered on nearest-neighbor equilateral triangles (NNETs), Mn-Mn bonds, and Mn atoms are used in conjunction with the shell model to simulate the intensity (as discussed in the Results section, and see figs. S12 to S14 without the shell model), and their optimal results are compared with the data. Note that an internal hollow structure of the magnetic clusters is necessary for producing the local maximum at Q_0, which is missing from calculations based on localized and delocalized electron clouds centered on Mn atoms (see the Results section and fig. S19). Error bars are statistical uncertainty 1 SD. (**B** to **E**) INS data in comparison with model calculations (see description in the Results section and the Supplementary Materials). Experimental results are obtained at E = 75 ± 10 meV and T = 4 K. (**F**) DFT-calculated magnetization densities in an atomic plane perpendicular to ⟨111⟩. Three neighboring Mn atoms are connected by an NNET (fig. S1). (**G**) The Mn sublattice, organized into NNETs with their four orientations indicated by colors. Highlighted atoms and bonds indicate a "trillium flower" (*41*) structural motif.

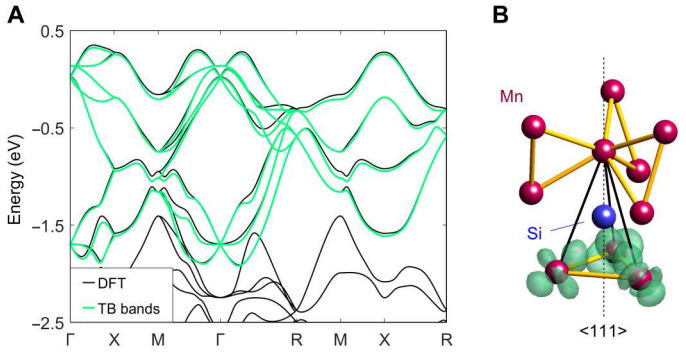

Fig. 4. Ab initio calculation of magnetic orbitals. (**A**) DFT-calculated bands near E_F in comparison to tight-binding (TB) models. The DFT result is consistent with previous calculation (*30*) and experiments (*31*, *61*). For clarity, only spin-majority bands are shown (minority bands in fig. S24). (**B**) MLWFs calculated from the EBR, resulting in molecular orbitals on NNETs. Isosurface (15% of maximum) of the electron density is shown on a structural motif highlighted in Fig. 3G. The spread of electron density $\langle r^2\rangle - \langle r\rangle^2$ (*4*) is 11.3 Å^2. The Mn atom above Si has AFM coupling (*38*) to those at the bottom, which translates into antiferromagnetic (AFM) coupling between neighboring triangles (Fig. 3G).

for them to be described by a stand-alone tight-binding model (*9*). We have performed an MLWF calculation restricted to the EBR. Consistent with the experiment, the obtained MLWFs are found to be centered on the triangles, and the resultant tight-binding model provides an excellent description of the magnetic bands (Fig. 4A). The high electron densities are around the Mn atoms and offset from the Wannier centers (Fig. 4B), a situation that closely resembles flat-band electrons in twisted bilayer graphene (*5*–*7*). Such a dichotomy between off-atom Wannier centers and atomic site–centered density islands is a consequence of the antibonding character of the conduction electrons (fig. S24), and it results in a "hollow" internal structure of the molecular orbitals that naturally explains the INS intensity's local maximum at Q_0 (Fig. 3A). We emphasize that these off-atom molecular orbitals constitute the most localized and physically relevant tight-binding basis for describing the magnetic electrons. In comparison, MLWFs obtained under Mn site constraint for the magnetic EBR (fig. S22D), or as atomic orbitals of Mn calculated without restriction to the EBR (fig. S22E), feature a substantially different shape of the electronic magnetization density, whose magnetic form factor is different from our experimental observation (Fig. 3A). More details on the comparison of different MLWFs can be found in the Supplementary Materials.

DISCUSSION

Our result brings critical insight into the magnetism of MnSi. We first note an intriguing similarity between the molecular orbitals' orientational characteristics, as seen from the INS continuum (Fig. 3, D and E), and those of spin correlations seen in MnSi's non–Fermi-liquid phase under pressure (*37*). The energy scale of the continuum is compatible with transitions of itinerant electrons (*30*–*33*), in the context of which our shell model would be an approximation for the (intra-BZ) joint density of states. The INS intensity further depends on transition matrix elements between the hybridized electronic states: As they all belong to the same magnetic EBR, the form factor of the triangles constitutes an excellent approximation for the intensity (see the Supplementary Materials for a mathematical proof that uses the localization property of MLWFs). Yet still, the continuum's persistence into the paramagnetic state is inconsistent with simple spin-polarized bands (*32*). Moreover, by accounting for the rapid form factor decrease toward large Q (fig. S16), we find a magnetic spectral weight of $\geq 2\mu_B^2/Mn$ for the continuum (see the Supplementary Materials), which is too large for purely itinerant excitations and suggests a dichotomy of itinerant and local moments.

From a local moment perspective, our result indicates that the fundamental magnetic units are molecular orbitals on the triangles, rather than Mn atoms (*38*–*40*). Compared to the shell model, the continuum can be nearly equally well described by a lattice Lorentzian model (fig. S18), which accounts for short-range antiferromagnetic (AFM) correlations. The MnSi structure's Wyckoff 4a site features a unique "trillium" lattice (*41*), where the proliferation of corner-sharing triangles (Figs. 3G and 4B) is expected to result in frustrated ordering in the case of AFM interactions, consistent with a low ordering temperature and reduced ordered moment per Mn (*42*–*44*). Both the Mn atom and the molecular orbital sites are Wyckoff 4a. Although either site can form a consistent tight-binding description of the magnetic EBR (fig. S22A), our INS data unequivocally indicate that the magnetization clouds are centered on the triangles. While nearest-neighbor Mn atoms are unlikely to have AFM coupling (*39*, *40*, *42*), an AFM coupling channel may exist between molecular orbitals on nearest-neighbor triangles because a pair of next–nearest-neighbor Mn atoms connected by a relatively straight Mn-Si-Mn bond, which has been proposed to produce (ionic) AFM coupling (*38*), are distributed at the far corners of such a pair of triangles (Figs. 3G and 4B). The associated pair of molecular orbitals are further expected to have magnetic coupling channels contributed by other pairs of Mn atoms, including the Hund's coupling on the Mn atom at the shared vertex. Our result motivates further study of magnetic couplings and correlations between molecular orbitals as the fundamental units.

The magnetic molecular orbitals further introduce an unexplored and interesting regime of the spin waves, where the wavelength becomes short and comparable to the spatial extent of the orbitals. Because the orbital's magnetization cloud must act together, spin waves in this regime are expected to become ill-defined (overdamped). For an estimate, by requiring the spin waves (as plane waves) to accommodate the circumcircle of the triangle into their amplitude profile's full width at half maximum, we obtain a cutoff momentum of $q_{MO} \approx 0.65$ Å^{-1}, which agrees well with our data in Fig. 1C and figs. S4 and S5: Propagating spin waves can hardly be observed beyond q_{MO}, where the scattering signal is dominated by the continuum. Instead of becoming overdamped, the spin waves might also pick up an extremely large dispersion velocity beyond q_{MO} because the molecular orbitals are highly rigid, but the signal's overlap with the continuum precludes a definitive answer at this point. Thus, while our finding does not rule out the conventional picture of magnon decay within a particle-hole continuum (*32*), it offers an alternative explanation for the disappearance of well-defined spin waves at short wavelengths. In the long-wavelength regime with $q \ll q_{MO}$, however, a molecular orbital description of the spin waves is not expected to be fundamentally different from an ionic picture. This is because, in both pictures, the spin precession can be regarded as uniform motion over distances much

greater than the size of the fundamental units. Moreover, the triangle and the atomic sites have exactly the same symmetry, such that all symmetry arguments (e.g., for Dzyaloshinskii-Moriya interactions) apply to both. Additional detailed discussions on these points can be found in the Supplementary Materials. Therefore, we believe that several important previous understandings of the low-energy physics (*29*, *36*, *45*, *46*) based on an ionic picture are equally compatible with our present molecular orbital picture.

To summarize, we have determined the electronic magnetization clouds in MnSi and found that they form magnetic molecular orbitals. The INS method works exceptionally well when the periodic intra-BZ and the global inter-BZ structures have separable momentum scales. Our concrete demonstration of magnetic molecular orbitals calls for an in-depth examination of this concept in many interesting but not fully understood quantum materials (*19*, *20*, *24*–*26*, *47*, *48*), where electron itinerancy and correlation are both significant, for which MLWF calculations (*5*, *8*, *21*, *49*) may provide important and potentially unexpected insights. The conceptual difference between molecular orbital and ionic magnetism is profound and independent of whether the system is metallic or insulating as per band filling. Notably, even if it was an insulator, MnSi would still escape recent high-throughput searches for molecular orbital materials (*11*, *12*) because both the Mn and the triangle sites share the same Wyckoff label. Last, we envision magnetic materials with topological bands to be an interesting frontier, where magnetic electrons cannot be described by exponentially localized Wannier orbitals (*9*, *10*). In such cases, one might not be able to decompose the magnetic neutron scattering cross section into form factor and spectral functions. A new description embracing the full wave-function structure of the magnetic electrons will be needed.

MATERIALS AND METHODS

Sample growth and characterization

High-quality single crystals of MnSi were grown in a mirror furnace (Quantum Design). Because MnSi melts congruently (*50*), no extra solvent was needed for the growth. Polycrystalline MnSi was synthesized by arc melting of high-purity raw materials (4N Mn and 6N Si), followed by suction casting into 5-mm-diameter rods inside a pure argon atmosphere. For a typical growth, the feed and seed rods were mounted and counterrotated between 17 and 25 rpm in a two-mirror image furnace (Quantum Design Inc.). The heating power was between 40 and 50% of the maximum level for the 650-W halogen lamps. Crystals were grown at a rate of 40 mm/hour and in pure argon flow. X-ray Laue backscattering from natural crystal surfaces produced sharp diffraction patterns with an approximate twofold symmetry (fig. S2A), consistent with the cubic space group $P2_13$ (no. 198; a = 4.556 Å). A total of 28 high-quality single crystals (total mass ≈ 33 g) were used for our experiments (fig. S2A). The crystals were coaligned on aluminum plates with a hydrogen-free adhesive, such that reciprocal lattice vectors (H, L, L) were in the horizontal plane. The (0, 3, 4) and (0, 4, 3) Bragg reflections differed in their intensities by a factor over 40, indicating that the entire sample was nearly a single domain (fig. S2, B and C). According to a rocking curve measured on the (2, 1, 1) nuclear Bragg reflection, the mosaic spread of the entire sample was about 1.3° (full width at half maximum; fig. S2D). Magnetometry measurements on a single crystal using a Quantum Design MPMS indicated a magnetic phase transition at 29.5 K and a saturated magnetic moment of 0.4 μ_B/Mn (fig. S2, E and F).

Inelastic neutron scattering

Our INS experiments were performed on the 4SEASONS spectrometer at the Material and Life Science Experimental Facility (MLF), Japan Proton Accelerator Research Complex (J-PARC), Japan, and the SEQUOIA and ARCS spectrometers at the Spallation Neutron Source, Oak Ridge National Laboratory, USA (*51*–*53*). The 4SEASONS spectrometer has a multiple-E_i capability, such that neutron scattering events with a series of different incident energies are recorded simultaneously. On the 4SEASONS spectrometer, a chopper frequency of 500 Hz was used for E_i = 22, 29, 40, 57, 90, and 162 meV, and measurements were performed at T = 4 and 40 K. On the SEQUOIA spectrometer, a chopper frequency of 600 Hz was used for E_i = 90 and 150 meV, and measurements were performed at T = 4, 40, and 300 K. On the ARCS spectrometer, chopper frequencies of 360, 540, and 600 Hz were used for E_i = 300, 600, and 1000 meV, respectively, and measurements were performed at T = 4 K. During the measurements, the sample was rotated about the vertical direction over a 40° range in 0.25° steps on 4SEASONS and over a 120° range in 1° steps on SEQUOIA and ARCS. Data accumulated at different angles were combined into a four-dimensional dataset, in which we used the Dave, Utsusemi, and Horace software packages for reduction and analysis (*54*–*56*). After a careful alignment of the measured dataset with the crystallographic coordinate system using all available nuclear Bragg reflections, the entire dataset was downfolded into a minimal, physically independent sector of the three-dimensional momentum space using the point-group symmetry of the system. The INS intensities were converted into absolute scattering cross sections by comparing to measurements of vanadium standard samples using exactly the same spectrometer conditions. The resultant cross sections were further corrected for neutron absorption, which is estimated to cause a minimum of 46% reduction of the scattering intensity based on the tabulated data on absorption cross sections for a neutron energy of 90 meV and with an effective sample thickness of 20 mm. Absorption-corrected absolute cross sections are presented throughout the manuscript.

Phonon calculations

The force constants of MnSi were calculated by the density functional perturbation theory with the Vienna Ab initio Simulation Package (VASP) (*57*, *58*). Perdew-Burke-Ernzerhof–type exchange-correlation functionals were adopted, within generalized gradient approximation regime (*59*). The kinetic energy cutoff was set to 400 eV. Integrations over BZ were performed with Monkhorst-Pack **Q**-point grid (equivalent to a 15 × 15 × 15 grid). Lattice constants and atomic positions were relaxed until residual forces drop below 0.001 eV/Å. The relaxed lattice constant was 4.42 Å, slightly smaller than our experimental value of 4.56 ± 0.01 Å as seen from the neutron diffraction results. The good agreement between the data and calculation shown in Fig. 1A enabled us to distinguish the spin waves from acoustic phonons by inspecting data acquired in different BZs (fig. S3) and to attribute scattering signals to magnetic excitations (i) below 20 meV near the BZ boundary, (ii) between 45 and 50 meV, and (iii) above 60 meV.

Electronic structure and MLWF calculations

The structure file of MnSi was downloaded directly from Materials Project website (*60*) with optimized lattice constant under given symmetries of space group no. 198. The projector augmented wave pseudopotentials Mn_sv_GW and Si_GW in VASP version 5.2 were adopted. The local density approximation exchange-correlation functional in accordance with the POTCAR file was used. The default setting was 11 by 11 by 11 for Monkhorst-Pack k-mesh size, 550 eV for cutoff energy of plane wave basis, and 1×10^{-6} for convergence tolerance of self-consistent total energy. The net magnetic moment size was fixed at the experimental value of 0.4 μ_B/Mn, following that in (*30*). We have performed convergence tests on the k-mesh size, the cutoff energy, and the convergence tolerance in the self-consistent calculations. Specifically, we have compared the converged total energy for various settings of a given parameter while fixing the other parameters to their default values. It is shown that the default settings reach a balance of efficiency and accuracy. Our DFT calculations in these settings are consistent with previous calculation (*30*) and experiments (*31*, *61*). We used Wannier90 to implement further calculations of MLWFs, following the optimization routine proposed by Marzari and Vanderbilt (*18*, *62*–*64*). MLWFs of the eight conduction bands near the Fermi energy were calculated. The disentanglement windows were adjusted to obtain high-quality MLWFs, and no frozen windows were used in disentanglement procedure. For additional detail and analyses of the results, see the Supplementary Materials.

Supplementary Materials

This PDF file includes:

Supplementary Text
Figs. S1 to S24
Tables S1 and S2
References

REFERENCES AND NOTES

1. K. Sato, L. Bergqvist, J. Kudrnovský, P. H. Dederichs, O. Eriksson, I. Turek, B. Sanyal, G. Bouzerar, H. Katayama-Yoshida, V. A. Dinh, T. Fukushima, H. Kizaki, R. Zeller, First-principles theory of dilute magnetic semiconductors. *Rev. Mod. Phys.* **82**, 1633–1690 (2010).
2. Y. O. Kvashnin, R. Cardias, A. Szilva, I. Di Marco, M. I. Katsnelson, A. I. Lichtenstein, L. Nordström, A. B. Klautau, O. Eriksson, Microscopic origin of Heisenberg and non-Heisenberg exchange interactions in ferromagnetic bcc Fe. *Phys. Rev. Lett.* **116**, 217202 (2016).
3. L. Pauling, The nature of the chemical bond. application of results obtained from the quantum mechanics and from a theory of paramagnetic susceptibility to the structure of molecules. *J. Am. Chem. Soc.* **53**, 1367–1400 (1931).
4. N. Marzari, A. A. Mostofi, J. R. Yates, I. Souza, D. Vanderbilt, Maximally localized Wannier functions: Theory and applications. *Rev. Mod. Phys.* **84**, 1419–1475 (2012).
5. H. C. Po, L. Zou, A. Vishwanath, T. Senthil, Origin of Mott insulating behavior and superconductivity in twisted bilayer graphene. *Phys. Rev. X* **8**, 031089 (2018).
6. M. Koshino, N. F. Q. Yuan, T. Koretsune, M. Ochi, K. Kuroki, L. Fu, Maximally localized Wannier orbitals and the extended hubbard model for twisted bilayer graphene. *Phys. Rev. X* **8**, 031087 (2018).
7. J. Kang, O. Vafek, Symmetry, maximally localized Wannier states, and a low-energy model for twisted bilayer graphene narrow bands. *Phys. Rev. X* **8**, 031088 (2018).
8. A. C. Walters, T. G. Perring, J.-S. Caux, A. T. Savici, G. D. Gu, C.-C. Lee, W. Ku, I. A. Zaliznyak, Effect of covalent bonding on magnetism and the missing neutron intensity in copper oxide compounds. *Nat. Phys.* **5**, 867–872 (2009).
9. B. Bradlyn, L. Elcoro, J. Cano, M. G. Vergniory, Z. Wang, C. Felser, M. I. Aroyo, B. A. Bernevig, Topological quantum chemistry. *Nature* **547**, 298–305 (2017).
10. H. C. Po, A. Vishwanath, H. Watanabe, Symmetry-based indicators of band topology in the 230 space groups. *Nat. Commun.* **8**, 50 (2017).
11. Y. Xu, L. Elcoro, Z.-D. Song, M. G. Vergniory, C. Felser, S. S. P. Parkin, N. Regnault, J. L. Mañes, B. A. Bernevig, Filling-enforced obstructed atomic insulators. arXiv:2106.10276 [cond-mat.mtrl-sci] (17 Jun 2021).
12. J. Gao, Y. Qian, H. Jia, Z. Guo, Z. Fang, M. Liu, H. Weng, Z. Wang, Unconventional materials: The mismatch between electronic charge centers and atomic positions. *Sci. Bull.* **67**, 598–608 (2022).
13. X.-P. Li, D.-S. Ma, C.-C. Liu, Z.-M. Yu, Y. Yao, From atomic semimetal to topological nontrivial insulator. *Phys. Rev. B* **105**, 165135 (2022).
14. J. P. Sheckelton, J. R. Neilson, D. G. Soltan, T. M. McQueen, Possible valence-bond condensation in the frustrated cluster magnet $LiZn_2Mo_3O_8$. *Nat. Mater.* **11**, 493–496 (2012).
15. H.-S. Kim, J. Im, M. J. Han, H. Jin, Spin-orbital entangled molecular J_{eff} states in lacunar spinel compounds. *Nat. Commun.* **5**, 3988 (2014).
16. D. I. Khomskii, S. V. Streltsov, Orbital effects in solids: Basics, recent progress, and opportunities. *Chem. Rev.* **121**, 2992–3030 (2021).
17. L. T. Nguyen, R. J. Cava, Hexagonal perovskites as quantum materials. *Chem. Rev.* **121**, 2935–2965 (2021).
18. N. Marzari, D. Vanderbilt, Maximally localized generalized Wannier functions for composite energy bands. *Phys. Rev. B* **56**, 12847–12865 (1997).
19. K. Tomiyasu, K. Iwasa, H. Ueda, S. Niitaka, H. Takagi, S. Ohira-Kawamura, T. Kikuchi, Y. Inamura, K. Nakajima, K. Yamada, Spin-orbit fluctuations in frustrated heavy-fermion metal LiV_2O_4. *Phys. Rev. Lett.* **113**, 236402 (2014).
20. I. I. Mazin, H. O. Jeschke, K. Foyevtsova, R. Valentí, D. I. Khomskii, Na_2IrO_3 as a molecular orbital crystal. *Phys. Rev. Lett.* **109**, 197201 (2012).
21. K. Foyevtsova, H. O. Jeschke, I. I. Mazin, D. I. Khomskii, R. Valentí, Ab initio analysis of the tight-binding parameters and magnetic interactions in Na_2IrO_3. *Phys. Rev. B* **88**, 035107 (2013).
22. S. Streltsov, I. I. Mazin, K. Foyevtsova, Localized itinerant electrons and unique magnetic properties of $SrRu_2O_6$. *Phys. Rev. B* **92**, 134408 (2015).
23. H. Takagi, T. Takayama, G. Jackeli, G. Khaliullin, S. E. Nagler, Concept and realization of Kitaev quantum spin liquids. *Nat. Rev. Phys.* **1**, 264–280 (2019).
24. C. M. Varma, Non-Fermi-liquid states and pairing instability of a general model of copper oxide metals. *Phys. Rev. B* **55**, 14554–14580 (1997).
25. X. Feng, K. Jiang, Z. Wang, J. Hu, Chiral flux phase in the Kagome superconductor AV_3Sb_5. *Sci. Bull.* **66**, 1384–1388 (2021).
26. I. Zaliznyak, A. T. Savici, M. Lumsden, A. Tsvelik, R. Hu, C. Petrovic, Spin-liquid polymorphism in a correlated electron system on the threshold of superconductivity. *Proc. Natl. Acad. Sci.* **112**, 10316–10320 (2015).
27. J. M. Tranquada, G. Xu, I. A. Zaliznyak, Magnetism and superconductivity in $Fe_{1+y}Te_{1-x}Se_x$. *J. Phys.: Condens. Matter* **32**, 374003 (2020).
28. G. Shirane, S. M. Shapiro, J. M. Tranquada, *Neutron Scattering with a Triple-Axis Spectrometer: Basic Techniques* (Cambridge University Press, 2002).
29. S. Mühlbauer, B. Binz, F. Jonietz, C. Pfleiderer, A. Rosch, A. Neubauer, R. Georgii, P. Böni, Skyrmion lattice in a chiral magnet. *Science* **323**, 915–919 (2009).
30. T. Jeong, W. E. Pickett, Implications of the B20 crystal structure for the magnetoelectronic structure of MnSi. *Phys. Rev. B* **70**, 075114 (2004).
31. M. A. Wilde, M. Dodenhöft, A. Niedermayr, A. Bauer, M. M. Hirschmann, K. Alpin, A. P. Schnyder, C. Pfleiderer, Symmetry-enforced topological nodal planes at the Fermi surface of a chiral magnet. *Nature* **594**, 374–379 (2021).
32. Y. Ishikawa, G. Shirane, J. A. Tarvin, M. Kohgi, Magnetic excitations in the weak itinerant ferromagnet MnSi. *Phys. Rev. B* **16**, 4956–4970 (1977).
33. A. Nicolaou, M. Gatti, E. Magnano, P. L. Fèvre, F. Bondino, F. Bertran, A. Tejeda, M. Sauvage-Simkin, A. Vlad, Y. Garreau, A. Coati, N. Guérin, F. Parmigiani, A. Taleb-Ibrahimi, Fermi surface symmetry and evolution of the electronic structure across the paramagnetic-helimagnetic transition in MnSi/Si(111). *Phys. Rev. B* **92**, 081110 (2015).
34. S. Bao, W. Wang, Y. Shangguan, Z. Cai, Z.-Y. Dong, Z. Huang, W. Si, Z. Ma, R. Kajimoto, K. Ikeuchi, S.-i. Yano, S.-L. Yu, X. Wan, J.-X. Li, J. Wen, Neutron spectroscopy evidence on the dual nature of magnetic excitations in a van der Waals metallic ferromagnet $Fe_{2.72}GeTe_2$. *Phys. Rev. X* **12**, 011022 (2022).
35. X. Chen, I. Krivenko, M. B. Stone, A. I. Kolesnikov, T. Wolf, D. Reznik, K. S. Bedell, F. Lechermann, S. D. Wilson, Unconventional Hund metal in a weak itinerant ferromagnet. *Nat. Commun.* **11**, 3076 (2020).
36. M. Janoschek, F. Bernlochner, S. Dunsiger, C. Pfleiderer, P. Böni, B. Roessli, P. Link, A. Rosch, Helimagnon bands as universal excitations of chiral magnets. *Phys. Rev. B* **81**, 214436 (2010).
37. C. Pfleiderer, D. Reznik, L. Pintschovius, H. v. Löhneysen, M. Garst, A. Rosch, Partial order in the non-Fermi-liquid phase of MnSi. *Nature* **427**, 227–231 (2004).
38. K. V. Shanavas, S. Satpathy, Electronic structure and the origin of the Dzyaloshinskii-Moriya interaction in MnSi. *Phys. Rev. B* **93**, 195101 (2016).
39. V. A. Chizhikov, V. E. Dmitrienko, Frustrated magnetic helices in MnSi-type crystals. *Phys. Rev. B* **85**, 014421 (2012).

40. V. E. Dmitrienko, V. A. Chizhikov, Weak antiferromagnetic ordering induced by Dzyaloshinskii-Moriya interaction and pure magnetic reflections in MnSi-type crystals. *Phys. Rev. Lett.* **108**, 187203 (2012).
41. J. M. Hopkinson, H.-Y. Kee, Geometric frustration inherent to the trillium lattice, a sublattice of the B20 structure. *Phys. Rev. B* **74**, 224441 (2006).
42. J. M. Hopkinson, H.-Y. Kee, Microscopic model for spiral ordering along (110) on the MnSi lattice. *Phys. Rev. B* **75**, 064430 (2007).
43. S. V. Isakov, J. M. Hopkinson, H.-Y. Kee, Fate of partial order on trillium and distorted windmill lattices. *Phys. Rev. B* **78**, 014404 (2008).
44. O. Janson, I. Rousochatzakis, A. A. Tsirlin, M. Belesi, A. A. Leonov, U. K. Rösler, J. van den Brink, H. Rosner, The quantum nature of skyrmions and half-skyrmions in Cu_2OSeO_3. *Nat. Commun.* **5**, 5376 (2014).
45. B. Roessli, P. Böni, W. E. Fischer, Y. Endoh, Chiral fluctuations in MnSi above the Curie temperature. *Phys. Rev. Lett.* **88**, 237204 (2002).
46. T. Weber, J. Waizner, P. Steffens, A. Bauer, C. Pfleiderer, M. Garst, P. Böni, Polarized inelastic neutron scattering of nonreciprocal spin waves in MnSi. *Phys. Rev. B* **100**, 060404 (2019).
47. R. Ballou, E. Lelièvre-Berna, B. Fåk, Spin fluctuations in $(Y_{0.97}Sc_{0.03})Mn_2$: A geometrically frustrated, nearly antiferromagnetic, itinerant electron system. *Phys. Rev. Lett.* **76**, 2125–2128 (1996).
48. K. Hattori, H. Tsunetsugu, Effective Hamiltonian of a three-orbital Hubbard model on the pyrochlore lattice: Application to LiV_2O_4. *Phys. Rev. B* **79**, 035115 (2009).
49. C. Lane, J. W. Furness, I. G. Buda, Y. Zhang, R. S. Markiewicz, B. Barbiellini, J. Sun, A. Bansil, Antiferromagnetic ground state of La_2CuO_4: A parameter-free *ab initio* description. *Phys. Rev. B* **98**, 125140 (2018).
50. H. Baker, Ed., *ASM Handbook, Volume 3: Alloy Phase Diagrams* (ASM International, 1992).
51. R. Kajimoto, M. Nakamura, Y. Inamura, F. Mizuno, K. Nakajima, S. Ohira-Kawamura, T. Yokoo, T. Nakatani, R. Maruyama, K. Soyama, K. Shibata, K. Suzuya, S. Sato, K. Aizawa, M. Arai, S. Wakimoto, M. Ishikado, S.-i. Shamoto, M. Fujita, H. Hiraka, K. Ohoyama, K. Yamada, C.-H. Lee, The Fermi chopper spectrometer 4SEASONS at J-PARC. *J. Phys. Soc. Jpn.* **80**, SB025 (2011).
52. G. E. Granroth, A. I. Kolesnikov, T. E. Sherline, J. P. Clancy, K. A. Ross, J. P. C. Ruff, B. D. Gaulin, S. E. Nagler, SEQUOIA: A newly operating chopper spectrometer at the SNS. *J. Phys. Conf. Ser.* **251**, 012058 (2010).
53. D. L. Abernathy, M. B. Stone, M. J. Loguillo, M. S. Lucas, O. Delaire, X. Tang, J. Y. Y. Lin, B. Fultz, Design and operation of the wide angular-range chopper spectrometer ARCS at the Spallation Neutron Source. *Rev. Sci. Instrum.* **83**, 015114 (2012).
54. R. T. Azuah, L. R. Kneller, Y. Qiu, P. L. W. Tregenna-Piggott, C. M. Brown, J. R. D. Copley, R. M. Dimeo, Dave: A comprehensive software suite for the reduction, visualization, and analysis of low energy neutron spectroscopic data. *J. Res. Natl. Inst. Stan. Technol.* **114**, 341–358 (2009).
55. Y. Inamura, T. Nakatani, J. Suzuki, T. Otomo, Development status of software "Utsusemi" for chopper spectrometers at MLF, J-PARC. *J. Phys. Soc. Jpn.* **82**, SA031 (2013).
56. R. A. Ewings, A. Buts, M. D. Le, J. van Duijn, I. Bustinduy, T. G. Perring, Horace: Software for the analysis of data from single crystal spectroscopy experiments at time-of-flight neutron instruments. *Nucl. Instrum. Methods Phys. Res. Sect.* **834**, 132–142 (2016).
57. X. Gonze, C. Lee, Dynamical matrices, born effective charges, dielectric permittivity tensors, and interatomic force constants from density-functional perturbation theory. *Phys. Rev. B* **55**, 10355–10368 (1997).
58. G. Kresse, J. Furthmüller, Efficient iterative schemes for ab initio total-energy calculations using a plane-wave basis set. *Phys. Rev. B* **54**, 11169–11186 (1996).
59. J. P. Perdew, K. Burke, M. Ernzerhof, Generalized gradient approximation made simple. *Phys. Rev. Lett.* **77**, 3865–3868 (1996).
60. A. Jain, S. P. Ong, G. Hautier, W. Chen, W. D. Richards, S. Dacek, S. Cholia, D. Gunter, D. Skinner, G. Ceder, K. A. Persson, The Materials Project: A materials genome approach to accelerating materials innovation. *APL Mater.* **1**, 011002 (2013).
61. Y. Fang, H. Zhang, D. Wang, G. Yang, Y. Wu, P. Li, Z. Xiao, T. Lin, H. Zheng, X.-L. Li, H.-H. Wang, F. Rodolakis, Y. Song, Y. Wang, C. Cao, Y. Liu, Quasiparticle characteristics of the weakly ferromagnetic Hund metal MnSi. *Phys. Rev. B* **106**, L161112 (2022).
62. A. A. Mostofi, J. R. Yates, Y.-S. Lee, I. Souza, D. Vanderbilt, N. Marzari, Wannier90: A tool for obtaining maximally-localised Wannier functions. *Comput. Phys. Commun.* **178**, 685–699 (2008).
63. G. Pizzi, V. Vitale, R. Arita, S. Blügel, F. Freimuth, G. Géranton, M. Gibertini, D. Gresch, C. Johnson, T. Koretsune, J. Ibañez-Azpiroz, H. Lee, J.-M. Lihm, D. Marchand, A. Marrazzo, Y. Mokrousov, J. I. Mustafa, Y. Nohara, Y. Nomura, L. Paulatto, S. Poncé, T. Ponweiser, J. Qiao, F. Thöle, S. S. Tsirkin, M. Wierzbowska, N. Marzari, D. Vanderbilt, I. Souza, A. A. Mostofi, J. R. Yates, Wannier90 as a community code: New features and applications. *J. Phys.: Condens. Matter* **32**, 165902 (2020).
64. I. Souza, N. Marzari, D. Vanderbilt, Maximally localized Wannier functions for entangled energy bands. *Phys. Rev. B* **65**, 035109 (2001).
65. A. Sapkota, L. Classen, M. B. Stone, A. T. Savici, V. O. Garlea, A. Wang, J. M. Tranquada, C. Petrovic, I. A. Zaliznyak, Signatures of coupling between spin waves and Dirac fermions in $YbMnBi_2$. *Phys. Rev. B* **101**, 041111 (2020).
66. Y. Li, N. Zaki, V. O. Garlea, A. T. Savici, D. Fobes, Z. Xu, F. Camino, C. Petrovic, G. Gu, P. D. Johnson, J. M. Tranquada, I. A. Zaliznyak, Electronic properties of the bulk and surface states of $Fe_{1+y}Te_{1-x}Se_x$. *Nat. Mater.* **20**, 1221–1227 (2021).
67. S. Toth, B. Lake, Linear spin wave theory for single-Q incommensurate magnetic structures. *J. Phys.: Condens. Matter* **27**, 166002 (2015).
68. G. Xu, Z. Xu, J. M. Tranquada, Absolute cross-section normalization of magnetic neutron scattering data. *Rev. Sci. Instrum.* **84**, 083906 (2013).
69. L. Elcoro, B. Bradlyn, Z. Wang, M. G. Vergniory, J. Cano, C. Felser, B. A. Bernevig, D. Orobengoa, G. de la Flor, M. I. Aroyo, Double crystallographic groups and their representations on the Bilbao Crystallographic Server. *J. Appl. Cryst.* **50**, 1457–1477 (2017).
70. J. Gao, Q. Wu, C. Persson, Z. Wang, Irvsp: To obtain irreducible representations of electronic states in the VASP. *Comput. Phys. Comm.* **261**, 107760 (2021).
71. M. G. Vergniory, L. Elcoro, C. Felser, N. Regnault, B. A. Bernevig, Z. Wang, A complete catalogue of high-quality topological materials. *Nature* **566**, 480–485 (2019).
72. V. P. Smirnov, D. E. Usvyat, Variational method for the generation of localized Wannier functions on the basis of Bloch functions. *Phys. Rev. B* **64**, 245108 (2001).
73. R. Sakuma, Symmetry-adapted Wannier functions in the maximal localization procedure. *Phys. Rev. B* **87**, 235109 (2013).
74. R. Dronskowski, P. E. Bloechl, Crystal orbital Hamilton populations (COHP): Energy-resolved visualization of chemical bonding in solids based on density-functional calculations. *J. Phys. Chem.* **97**, 8617–8624 (1993).
75. E. V. Komleva, D. I. Khomskii, S. V. Streltsov, Three-site transition-metal clusters: Going from localized electrons to molecular orbitals. *Phys. Rev. B* **102**, 174448 (2020).
76. J. F. Cooke, Neutron scattering from itinerant-electron ferromagnets. *Phys. Rev. B* **7**, 1108–1116 (1973).
77. J. H. Wernick, G. K. Wertheim, R. C. Sherwood, Magnetic behavior of the monosilicides of the 3d-transition elements. *Mat. Res. Bull.* **7**, 1431–1441 (1972).

Acknowledgments: We are grateful for discussions with G. Chen, J. Feng, J. Kang, W. Ku, Z. Liu, Z. Lu, Z. Song, Y. Wan, F. Wang, and Y. Yao. Yuan Li thanks the Tsung-Dao Lee Institute at Shanghai Jiao Tong University for hospitality during the preparation of the manuscript. **Funding:** Yuan Li acknowledges support by the National Key R&D Program of China (no. 2018YFA0305602) and the National Natural Science Foundation of China (nos. 12061131004 and 11888101). B.W. acknowledges support by the National Key R&D Program of China (nos. 2017YFA0303302 and 2018YFA0305602), the National Natural Science Foundation of China (no. 11921005), and the Shanghai Municipal Science and Technology Major Project (no. 2019SHZDZX01). The work at Brookhaven National Laboratory was supported by the Office of Basic Energy Sciences (BES), Division of Materials Sciences and Engineering, U.S. Department of Energy (DOE), under contract DE-SC0012704. Part of this research was performed at the MLF, J-PARC, Japan, under a user program (proposal no. 2019A0085). A portion of this research used resources at the Spallation Neutron Source, a DOE Office of Science User Facility operated by the Oak Ridge National Laboratory. **Author contributions:** Yuan Li conceived the research. Z.J., Yangmu Li, and Yuan Li designed the experiments. Z.J., B.H., X.Z., H.C., and Y.W. synthesized the crystals. Z.J. and B.H. characterized and prepared the INS sample. Z.J., Yangmu Li, B.H., I.A.Z., and Yuan Li performed the INS experiments with the assistance from K.I., K.K., M.B.S., A.I.K., and D.L.A. Z.J., Yangmu Li, I.A.Z., J.M.T., and Yuan Li analyzed the experimental data. Z.H. and B.W. performed the MLWF calculations. Yiran Liu and C.F. performed the phonon calculations. Z.J., Yangmu Li, Z.H., and Yuan Li wrote the manuscript with input from all coauthors. **Competing interests:** The authors declare that they have no competing interests. **Data and materials availability:** All data needed to evaluate the conclusions in the paper are present in the paper and/or the Supplementary Materials. The data can be accessed at https://figshare.com/articles/dataset/MnSi_manuscript_data_code/21203807.

Submitted 16 June 2022
Accepted 30 November 2022
Published 4 January 2023
10.1126/sciadv.add5239